


## Valley filtering in graphene under a magnetic proximity

Jianlong Zheng, Junqiang Lu, and Feng Zhai\*

*Department of Physics, Zhejiang Normal University, Jinhua 321004, China*

 (Received 14 November 2021; revised 7 February 2022; accepted 28 March 2022; published 11 April 2022)

We investigate valley-dependent electronic transport properties of graphene in close proximity to a thick ferromagnetic insulator (FI). It is found that spin-resolved valley filtering can be achieved under the interplay between the stray field emanated from the FI and the exchange-proximity interaction. In the intraband-tunneling regime, there exists a window of Fermi energy where both the spin and valley polarization of the output current are almost complete ( $\approx -100\%$ ). In the interband-tunneling regime, the valley polarization can approach 100% or  $-70\%$  near some conductance peaks, while the spin polarization is near 100% in a wide window of Fermi energy. The role of valley-Zeeman coupling is examined for both cases. The spin-valley filtering is found to be tunable by electric gating. Our findings are helpful for designing a spin-valley filter based on graphene with imprinted ferromagnetism.

DOI: [10.1103/PhysRevB.105.165410](https://doi.org/10.1103/PhysRevB.105.165410)

### I. INTRODUCTION

The exploration of graphene spintronics has attracted great interest in recent years. Pristine graphene is nonmagnetic and has rather weak spin-orbit and hyperfine interactions [1,2]. It thus stands as a promising spin-channel material. The incorporation of magnetism into graphene offers an opportunity to design graphene-based spin-logic devices [3–27]. The ferromagnetic order in graphene can be imprinted by means of defects such as adatoms [9] and vacancies [10], zigzag edges [11], and exchange-proximity interaction [4,7,12–17]. For the last method, a ferromagnetic insulator (FI) or ferrimagnetic one is placed on the top/bottom of graphene so that the  $p_z$  orbitals of electrons in graphene hybrid with  $d$  or  $f$  orbitals of neighboring magnetic ions [18–20]. Such an approach could remain the excellent transport properties of graphene [7]. The proximity-induced ferromagnetism is expected to bring novel transport phenomena in graphene such as the quantized anomalous Hall effect [7], giant proximity magnetoresistance [21–23], and chiral charge pumping [24]. It was reported experimentally that in a EuS/graphene system [25] the proximity-induced exchange fields can approach 100 T. For a graphene-based system with yttrium iron garnet (YIG) substrate, nonlocal spin-transport measurements [18] demonstrated an exchange field strength of 0.2 T. The deposition of EuO on graphene was experimentally realized and its proximity-induced ferromagnetism was confirmed [17,26,27].

Detailed *ab initio* calculations [8] revealed an intricate form of the proximity exchange interaction. For electrons in graphene, the effective Hamiltonian around the  $\mathbf{K}$  and  $\mathbf{K}'$  valleys includes not only the exchange splitting, but also a spin-dependent mass term and gap opening. The model parameters vary with the layer thickness of the neighboring FI film, which saturate for several bilayers of FI. For a thick

FI, the stray field due to the magnetization inevitably affects the motion of electrons in graphene. Such a local magnetic field was neglected in previous studies [4,15,21–23]. In the presence of gap opening, it can couple with the orbital magnetic moment induced by the Berry curvature, leading to a valley-Zeeman coupling [28–31]. The two-fold valley degeneracy [32] of electrons in graphene was utilized to construct carbon-based electronic devices with spintronic analogies. For this valleytronics routine a necessary step is to create an imbalanced valley population [33] such as valley spatial separation and valley-polarized current. To this end various valley-related effects are utilized, such as valley selection by tailored edges [34], valley-dependent group velocity [35] due to trigonal warping of energy bands, strain-induced pseudomagnetic fields [36], sublattice-staggered potential [37], valley asymmetry in light-induced quasienergy bands [38], and tunneling from two- to three-dimensional massless Dirac fermions [39]. To our knowledge, valley filtering in graphene under a magnetic proximity has not been studied.

In this work we present a thorough study on the spin and valley transport for graphene electrons in proximity to a thick FI (EuO). The effect of stray field emanated from the FI is considered. The proximity exchange interactions leads to a sublattice-staggered potential and a spin-dependent gap opening. It is found that significant spin-resolved valley filtering can be achieved under the interplay between the stray field and these proximity effects. The valley polarization of output current can be controllable by voltage gates and is more remarkable in the interband-tunneling transport regime.

### II. MODEL AND FORMALISM

The considered system is schematically shown in Fig. 1(a), where a EuO layer is deposited on a graphene membrane in the  $xy$  plane to induce a magnetic proximity effect. The FI EuO has magnetization  $M$  along the  $z$  axis. Carriers in the graphene have a conserved spin  $z$  component. In a stripe

\*fzhai@zjnu.cn

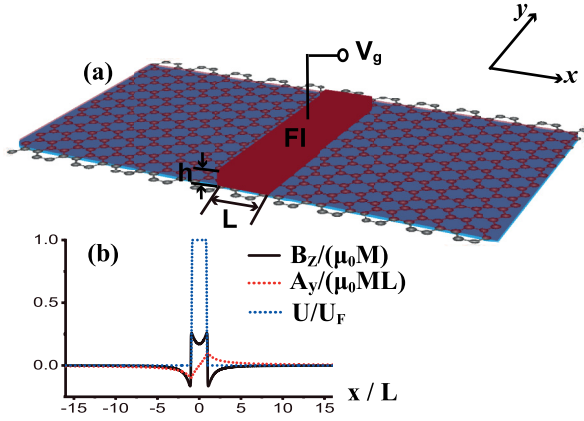


FIG. 1. (a) Schematic diagram for the proposed valley filter based on graphene under magnetic proximity. The FI on top of graphene is thick (with height  $h$  and magnetization  $M\mathbf{e}_z$ ) in the region  $|x| < L/2$  and thin otherwise. A metallic gate is further deposited on its thick part. (b) Profiles of field and potential in the graphene including perpendicular magnetic field  $B_z$  generated by the FI (black solid line), vector potential  $A_y$  in the Landau gauge (red dashed line), and electric potential  $U$  (with maximum  $U_F$ ) generated by top gate (blue dash-dotted line).

region  $|x| < L/2$ , the thickness  $h$  of the EuO layer is large so that an inhomogeneous magnetic field  $\mathbf{B}(\mathbf{r})$  is formed in the underlying graphene plane. This kind of local magnetic field is called the magnetic barrier, which has been formed experimentally on conventional two-dimensional electron gas [40–43]. A metallic gate on top of this thick EuO layer is used to create an electrostatic potential  $U(\mathbf{r})$ . Outside this stripe region, the EuO layer is thin. In the graphene plane, both the fringe field  $\mathbf{B}(\mathbf{r})$  and the electrostatic potential  $U(\mathbf{r})$  varies only along the  $x$  direction. The Landau gauge is taken for the vector potential,  $\mathbf{A}(\mathbf{r}) = A_y(x)\mathbf{e}_y$  with  $A_y(x) = \int_0^x B_z(x')dx'$ . Away from the stripe region,  $\mathbf{A}(\mathbf{r})$  tends to be constant and  $U(\mathbf{r}) = 0$ . The profile of magnetic field and vector potential are shown in Fig. 1(b), which read [44]

$$\begin{aligned} B_z &= \frac{\mu_0 M}{4\pi} \left[ C_1 \left( x + \frac{L}{2} \right) - C_1 \left( x - \frac{L}{2} \right) \right], \\ C_1(x) &= -2 \left( \arctan \frac{x}{z_0 + h} - \arctan \frac{x}{z_0} \right), \\ A_y(z) &= \frac{\mu_0 M}{4\pi} \left[ C_2 \left( x + \frac{L}{2} \right) - C_2 \left( x - \frac{L}{2} \right) \right], \\ C_2(x) &= \left[ z \ln(x^2 + z^2) - 2x \arctan \frac{x}{z} \right] \Big|_{z=z_0}^{z=z_0+h}, \end{aligned} \quad (1)$$

where  $z_0$  is the distance between graphene and the bottom of FI.

For an electron with spin  $s \in \{\uparrow, \downarrow\}$  in the graphene plane, the low-energy effective Hamiltonian can be written as [8,15,19]

$$\hat{H}_{\tau,s} = v_s \hat{\sigma} \cdot (\hat{\mathbf{p}} + e\mathbf{A}) + \tau \frac{\Delta_s}{2} \hat{\sigma}_z + (D_s + U) \hat{\sigma}_0. \quad (2)$$

Here  $\tau = \pm 1$  designates the two valleys  $\mathbf{K}$  and  $\mathbf{K}'$ ;  $v_s$ ,  $\Delta_s$ , and  $D_s$  are, respectively, the spin-dependent Fermi velocity,

gap opening, and energy shift of Dirac point;  $\hat{\sigma} = (\hat{\sigma}_x, \hat{\sigma}_y, \hat{\sigma}_z)$  consists of three Pauli matrices;  $\hat{\sigma}_0$  is a unit matrix; and  $\hat{\mathbf{p}} = -i\hbar(\partial_x, \partial_y)$  is the two-dimensional momentum operator. The second term in Eq. (2) is the sublattice-staggered potential. The magnetic proximity also brings a spin-independent energy shift of Dirac point, which is uniform in the system and is thus omitted. In Eq. (2) we also neglect the spin-Zeeman term  $\hat{H}^{SZ} = g\mu_B \hat{\sigma} \cdot \mathbf{B}/2$ , where  $\mu_B = 5.788 \times 10^{-2}$  meV/T is the Bohr magneton and  $g \approx 2$  is the g-factor. For a magnetic field  $B = 1$  T, the magnitude of spin-Zeeman splitting  $g\mu_B B$  is lower than 0.12 meV.

The valley-Zeeman term [30,31] was utilized to achieve valley-selective transmission in gapped bilayer graphene. It arises from the orbital magnetic moment of a topological nature. In the absence of magnetic-electric barrier ( $\mathbf{A} = U = 0$ ), the eigenstate of  $\hat{H}_{\tau,s}$  with conserved momentum  $\mathbf{p} = \hbar\mathbf{k}$  has the form  $u_{\mathbf{k}} \exp(i\mathbf{k} \cdot \mathbf{r})$  with  $u_{\mathbf{k}}^\dagger u_{\mathbf{k}} = 1$  and energy

$$E_{\mathbf{k}} = D_s \pm \sqrt{(\hbar v_s k)^2 + (0.5\Delta_s)^2}. \quad (3)$$

The orbital magnetic moment  $\mathbf{m}$  for an electron in this eigenstate is along the  $z$  axis and has a nonzero component [45]

$$m_z = \frac{e}{\hbar} \langle \partial_{k_x} u | \hbar v_s \hat{\sigma} \cdot \mathbf{k} + \tau \frac{\Delta_s}{2} \hat{\sigma}_z + (D_s - E_{\mathbf{k}}) \hat{\sigma}_0 | \partial_{k_y} u \rangle. \quad (4)$$

After some algebra, we get

$$m_z = \left( \frac{0.5\Delta_s}{E_{\mathbf{k}} - D_s} \right)^2 m_{z0}, \quad m_{z0} = \frac{-e\hbar v_s^2}{\tau \Delta_s}. \quad (5)$$

For  $v_s \approx 10^6$  m/s and  $\Delta_s \approx 100$  meV,  $|m_{z0}| \approx 6.6$  meV/T is about  $114 \mu_B$ . In bilayer (trilayer) graphene under vertical electric fields [28,29] the measured orbital magnetic moment can exceed  $10^2 \mu_B$  ( $10^3 \mu_B$ ). For an electron in valley  $\tau$  with energy  $E$  and spin  $s$ , the magnetic proximity also leads to a valley-Zeeman coupling

$$\hat{H}_{\tau,s}^{VZ} = \tau U_m \hat{\sigma}_0, \quad U_m = B_z |m_{z0}| F \left( \left| \frac{E - D_s}{0.5\Delta_s} \right| \right), \quad (6)$$

$$F(X) = X^{-2} \Theta(X - 1), \quad (7)$$

where  $\Theta(X)$  is the Heaviside step function. This term depends on both the spin and valley index, which vanishes inside the lead region where  $B_z(x) = 0$ .

For silicene in close proximity to a FI, valley and spin filtering were studied in Refs. [46–48] by means of an effective Hamiltonian similar to Eq. (2). A distinction between silicene and graphene is that in silicene the intrinsic spin-orbit coupling is large and the band gap can be tuned by gate voltages. In these studies the FI were assumed to provide only the exchange-splitting field [corresponding to the  $D_s \hat{\sigma}_0$  term in Eq. (2)]. In Eq. (2) the FI also brings a magnetic field and spin-resolved band gap  $\Delta_s$  and Fermi velocity  $v_s$ .

The momentum component  $\hat{p}_y$  commutes with the total Hamiltonian  $\hat{H}_{\tau,s} + \hat{H}_{\tau,s}^{VZ}$  and is thus conserved. The scattering state for an incident electron with energy  $E$  and transverse momentum  $p_y = \hbar q$  can be written as  $\exp(iqy)\psi_{\tau,s}^q(x)$ , where

$\psi_{\tau,s}^q(x)$  satisfies a reduced one-dimensional Schrödinger equation

$$\left\{ -i\partial_x \hat{\sigma}_x + \left[ q + \frac{e}{\hbar} A_y(x) \right] \hat{\sigma}_y + \frac{U(x) + \tau U_m(x)}{\hbar v_s} \hat{\sigma}_0 + \frac{0.5\tau \Delta_s}{\hbar v_s} \hat{\sigma}_z \right\} \psi_{\tau,s}^q(x) = \frac{E - D_s}{\hbar v_s} \psi_{\tau,s}^q(x). \quad (8)$$

The incident and outgoing wave can be written as

$$\begin{aligned} \psi_{\tau,s}^{q,i}(x) &= \begin{pmatrix} Q_{\tau,s} \\ k_{-\infty}^{+q} \end{pmatrix} e^{ik_{-\infty}x} + r_{\tau,s} \begin{pmatrix} Q_{\tau,s} \\ -k_{-\infty}^{-q} \end{pmatrix} e^{-ik_{-\infty}x}, \\ \psi_{\tau,s}^{q,o}(x) &= t_{\tau,s} \begin{pmatrix} Q_{\tau,s} \\ k_{+\infty}^{+q} \end{pmatrix} e^{ik_{+\infty}x}, \end{aligned} \quad (9)$$

where the longitudinal wave vector  $k_{\pm\infty}$  is real

$$Q_{\tau,s} = \frac{E + 0.5\tau \Delta_s - D_s}{\hbar v_s}, \quad (10)$$

$$\frac{k_{\pm\infty}}{\text{sgn}(Q_{\tau,s})} = \sqrt{\left( \frac{E - D_s}{\hbar v_s} \right)^2 - \left( \frac{0.5\Delta_s}{\hbar v_s} \right)^2 - q_{\pm\infty}^2}, \quad (11)$$

$$q_{\pm\infty} = q + eA_y(\pm\infty)/\hbar, \quad (12)$$

$$k_{a\infty}^{\pm q} = k_{a\infty} \pm iq_{a\infty}, \quad a \in \{+, -\}. \quad (13)$$

Generally, the reflection and transmission coefficient ( $r_{\tau,s}$  and  $t_{\tau,s}$ ) can be calculated numerically by means of the scattering matrix method [49,50]. The transmission probability  $T_{\tau,s} = |k_{+\infty}/k_{-\infty}| |t_{\tau,s}|^2$  depends on the incident energy  $E$  and transverse wave vector  $q$ .

The valley-related and spin-resolved conductance at zero temperature is determined by the Landauer-Büttiker formula

$$G_{\tau,s}(E_F) = G_0 \int T_{\tau,s}(E_F, q) dq. \quad (14)$$

Here  $E_F$  is the Fermi energy,  $G_0 = e^2 L_y / (4\pi^2 \hbar)$ , and  $L_y$  is the transverse length of the sample. Once  $G_{\tau,s}$  is obtained, the total conductance  $G_T$ , valley conductance  $G_V$ , and spin conductance  $G_S$  are calculated straightforwardly

$$G_T = G_{+\uparrow} + G_{-\uparrow} + G_{+\downarrow} + G_{-\downarrow}, \quad (15)$$

$$G_V = G_{+\uparrow} + G_{+\downarrow} - G_{-\uparrow} - G_{-\downarrow}, \quad (16)$$

$$G_S = G_{+\uparrow} + G_{-\uparrow} - G_{+\downarrow} - G_{-\downarrow}. \quad (17)$$

The valley (spin) polarization  $P_V$  ( $P_S$ ) can be characterized by the ratio between the valley (spin) conductance and total conductance

$$P_V = \frac{G_V}{G_T}, \quad P_S = \frac{G_S}{G_T}. \quad (18)$$

To demonstrate the working principle of the proposed device, we also consider a rectangular magnetic barrier with height  $B > 0$  and a rectangular electric barrier with height  $U$  within the stripe  $|x| < L/2$ , for which one can work out the transmission probability  $T_{\tau,s}$ . In this case

$$B_z(\mathbf{r}) = B\Theta\left(\frac{L^2}{4} - x^2\right), \quad U(\mathbf{r}) = U\Theta\left(\frac{L^2}{4} - x^2\right). \quad (19)$$

Accordingly,  $A_y(x) = Bx$  for  $|x| < L/2$  and  $A_y(\pm\infty) = \pm BL/2$ . In the stripe region, the solution of Eq. (8) admits

the form

$$\psi_{\tau,s}^{q,m}(x) = c_1 \begin{pmatrix} \gamma D_{p-1}(X) \\ D_p(X) \end{pmatrix} + c_2 \begin{pmatrix} -\gamma D_{p-1}(-X) \\ D_p(-X) \end{pmatrix}, \quad (20)$$

where  $c_1$  and  $c_2$  are unknown constants,  $X = \sqrt{2}(x/l_B + ql_B)$  with  $l_B = [\hbar/(eB)]^{1/2}$ ,  $D_\alpha(X)$  is the parabolic cylinder function [51] of order  $\alpha$ ,

$$p = \frac{(E - D_s - U_T)^2 - (0.5\Delta_s)^2}{2(\hbar v_s/l_B)^2}, \quad (21)$$

$$U_T = \tau B \frac{e\hbar v_s^2}{\Delta_s} F\left(\left|\frac{E - D_s}{0.5\Delta_s}\right|\right) + U, \quad (22)$$

$$\gamma = \frac{-iE + 0.5\tau \Delta_s - D_s - U_T}{\sqrt{2} \hbar v_s/l_B}, \quad (23)$$

and  $F(X)$  is the function defined in Eq. (7). By matching the wave function  $\psi_{\tau,s}^{q,m}$  and  $\psi_{\tau,s}^{q,i}$  ( $\psi_{\tau,s}^{q,o}$ ) at  $x = -L/2$  ( $x = L/2$ ), we yield

$$T_{\tau,s} = \frac{4k_{+\infty}k_{-\infty}(D_{p-1}^{+r}D_p^{-r} + D_{p-1}^{-r}D_p^{+r})^2}{|k_{-\infty}^{-q}I_{p-1}^p + k_{+\infty}^{+q}I_p^{p-1} - i\Omega I_p^p + i\omega I_{p-1}^{p-1}|^2}. \quad (24)$$

Here  $k_{\pm\infty}$ ,  $k_{-\infty}^{-q}$ , and  $k_{+\infty}^{+q}$  are given in Eqs. (11) to (13),  $D_\alpha^{\pm l} = D_\alpha(\pm X_l)$  with  $X_l = \sqrt{2}(-0.5L/l_B + ql_B)$ ,  $D_\alpha^{\pm r} = D_\alpha(\pm X_r)$  with  $X_r = \sqrt{2}(0.5L/l_B + ql_B)$ ,

$$I_\alpha^\beta = D_\alpha^{-l}D_\beta^{+r} - (-1)^{\alpha-\beta}D_\alpha^{+l}D_\beta^{-r}, \quad (25)$$

$$\Omega = \frac{\sqrt{2}}{l_B} \frac{E + 0.5\tau \Delta_s - D_s}{E + 0.5\tau \Delta_s - D_s - U_T}, \quad (26)$$

$$\omega = \frac{k_{-\infty}^{-q}k_{+\infty}^{+q}}{\Omega}. \quad (27)$$

The Landau levels in the barrier region can be obtained from Eq. (20) with the requirement  $\psi_{\tau,s}^{q,m}(x = \pm\infty) = 0$ . The equivalent condition is that  $p$  in Eq. (21) is a positive integer  $n$  or  $p = \gamma = 0$  so that

$$(E - D_s - U_T)^2 = (0.5\Delta_s)^2 + 2neB\hbar v_s^2, \quad n \geq 0. \quad (28)$$

For the positive integer  $n$ , the Landau level  $E_n^{c,v}$  derived from the conduction/valence band is determined from Eq. (28) and can be written as

$$E_n^{c,v} = 0.5\Delta_s x_n^{c,v} + U + D_s. \quad (29)$$

Here  $x_n^{c,v}$  is the real root of the polynomial

$$x^3 \mp \frac{\sqrt{(0.5\Delta_s)^2 + 2neB\hbar v_s^2}}{0.5\Delta_s} x^2 - \frac{\tau B|m_{z0}|}{0.5\Delta_s} \quad (30)$$

and satisfies  $x_n^c > 1$  and  $x_n^v < -1$ . The special zeroth Landau level [52,53] is determined by  $p = \gamma = 0$  and always valley-dependent

$$E_0 = -0.5\tau \Delta_s + U + D_s. \quad (31)$$

Without the valley-Zeeman term ( $m_{z0} = 0$ ), the Landau level with index  $n > 0$  becomes valley-degenerate

$$E_{n0}^{c,v} = \pm \sqrt{(0.5\Delta_s)^2 + 2neB\hbar v_s^2} + U + D_s. \quad (32)$$

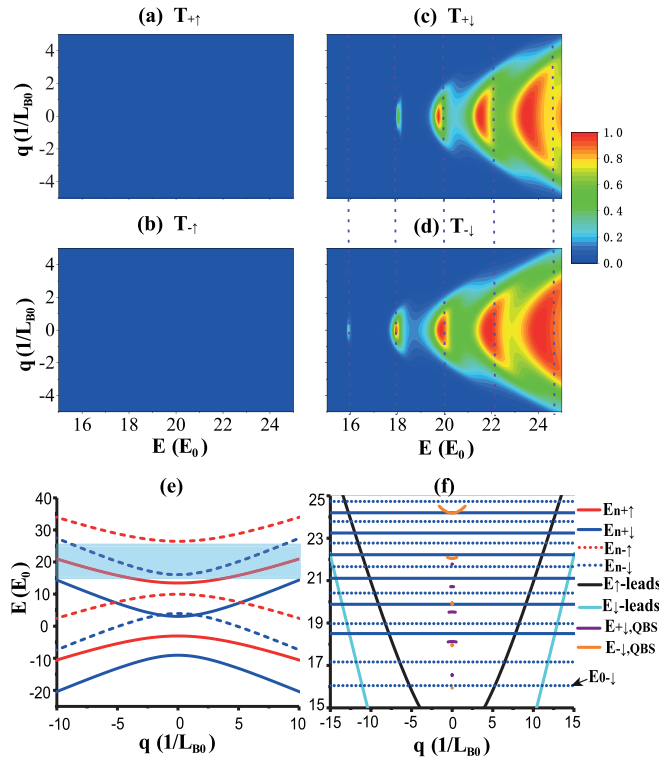


FIG. 2. Contour plots of valley-dependent transmission  $T_{\tau, \uparrow/\downarrow}$  as functions of incident energy  $E$  and transverse wave vector  $q$  for (a,b) spin-up and (c,d) spin-down electrons. The transmission  $T_{\tau, \uparrow/\downarrow}$  is calculated by Eq. (24) for a rectangular magnetic-electric barrier with parameters  $B = 5$ ,  $L = 2$ , and  $U = 13$ . (e) Band dispersion near energy zero for spin-up (red curves) and spin-down (blue curves) electrons in graphene under magnetic proximity. Dispersion in leads given in Eq. (3) is plotted in solid lines. Within the barrier region, the dispersion under  $B_z = 0$  is plotted in dotted lines. The shadowed region indicates the considered energy regime in (a)–(d). (f) Landau levels [given by Eqs. (29)–(31)] in the middle region and dispersion in leads and quasibound states within the energy interval  $15 < E < 25$ .  $E_{n, \tau, s}$  is the  $n$ th Landau level for electrons in valley  $\tau$  with spin  $s$ . The dispersion of quasibound states  $E_{\pm, \downarrow, QBS}$  are concentrated at  $q = 0$ .

For a finite barrier width, there exist quasibound states derived from these Landau levels. The wave function for a quasibound state with energy  $E$  and transverse wave vector  $q$  is given by Eqs. (9) and (20) with  $r_{\tau, s} = 0$ , or equivalently, perfect transmission [54]  $T_{\tau, s} = 1$ .

### III. RESULTS AND DISCUSSIONS

The parameters for graphene under the proximity of EuO FI are taken as [8, 15, 20, 22]  $\Delta_{\uparrow} = 134$  meV,  $\Delta_{\downarrow} = 98$  meV,  $D_{\uparrow} = 42$  meV,  $D_{\downarrow} = -24$  meV,  $v_{\uparrow} = 1.34 \times 10^6$  m/s, and  $v_{\downarrow} = 1.63 \times 10^6$  m/s. For convenience, hereafter we take a typical magnetic field  $B_0 = 0.1$  T and velocity  $v_0 = 10^6$  m/s so that the length and energy are, respectively, in units of  $l_{B0} = [\hbar/(eB_0)]^{1/2} = 81.1$  nm and  $E_0 = \hbar v_0/l_{B0} = 8.1$  meV.

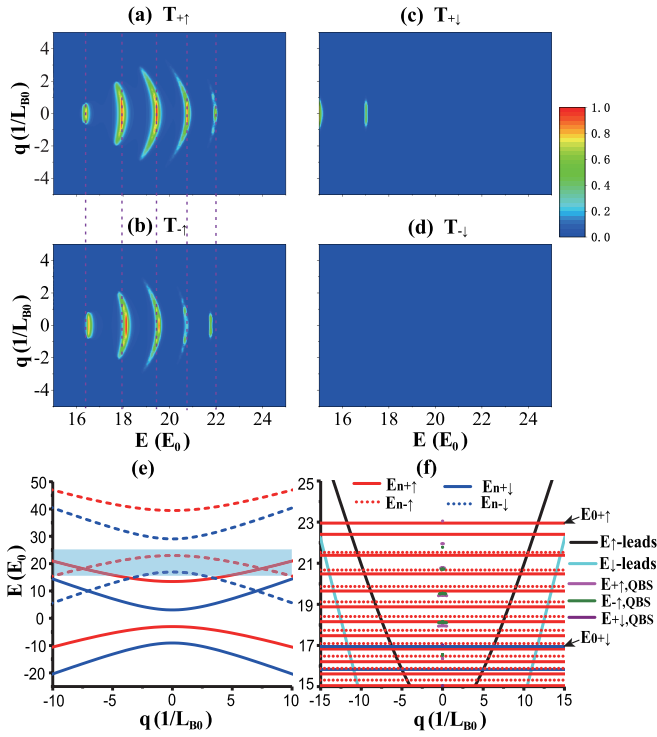
For a rectangular magnetic-electric barrier, the spin- and valley-resolved transmission probability  $T_{\tau, s}$  is calculated from Eq. (24) and plotted in Fig. 2 for the electric barrier

height  $U = 13$ . The height and width of the magnetic barrier are fixed at  $B = 5 B_0$  and  $L = 2$ . In the considered energy regime ( $15 < E < 25$ ), the transmission probabilities of spin-up electrons are almost zero [see Figs. 2(a) and 2(b)]. For spin-down electrons in either valley [see Figs. 2(c) and 2(d)], a series of resonant peaks are observed in the transmission spectrum for the normal incidence ( $q = 0$ ). The transmission is symmetric about the line  $q = 0$ . The locations of transmission peaks depends on the valley index, as guided by the vertical dashed lines. With the increase of incident energy  $E$ , the transmission is visible in a more broad interval of transverse wave vector  $q$ . In addition, near  $E = 16$  electrons in  $\mathbf{K}$  valley are almost totally reflected, while electrons in the  $\mathbf{K}'$  valley shows a noticeable transmission near  $q = 0$ . Consequently, a remarkable valley contrast can be expected for incident energy near this energy and near valley-resolved resonant peaks.

In Fig. 2(e) the band dispersion around energy zero is plotted as solid lines for the lead region. In the considered energy regime (shadowed part), propagating modes in leads come from the two spin-resolved conduction bands. In the barrier region under  $B_z = 0$ , the spin-up bands (red dashed lines) are outside the shadowed energy interval, while the spin-down conduction band covers this energy regime. As a result, the spin-up transmission shown in Figs. 2(a) and 2(b) is suppressed. Under a finite  $B_z = 0.5$  T, the spin-down conduction band in the barrier region has a valley splitting  $\approx 9$  meV. The intraband tunneling is thus valley-dependent. In Fig. 2(f), the Landau levels in the middle region are plotted. Within the energy interval  $15 < E < 25$ , the Landau levels are derived only from the spin-down conduction band. The valley splitting of these Landau levels  $E_{n, \pm \downarrow}$  arises from the valley-Zeeman term in Eq. (6), which decreases with the index  $n$ . All perfect transmission peaks in Figs. 2(c) and 2(d) are close to some Landau levels in Fig. 2(f). The first resonant peak in Fig. 2(d) is very close to the zeroth Landau level  $E_{0, -\downarrow}$ . Actually, each of these resonant peaks results from a quasibound state with energy derived from one or a pair of Landau levels. The dispersion of quasibound states is also plotted in Fig. 2(f), which is almost flat and concentrated at  $q = 0$ . In Eq. (24), the valley dependence of transmission arises from the valley-Zeeman coupling [31] (through  $p$  and  $\Omega$ ) and intrinsic valley splitting induced by the magnetic-electric barrier alone [37] (through  $\Omega$ ). The valley contrast can be controlled by the parameter  $\Omega$  defined in Eq. (26), where a proper electric barrier  $U$  can enhance the valley contrast in Figs. 2(c) and 2(d).

By varying the height of electric barrier, one can turn the transport from the intraband-tunneling regime (in Fig. 2) to the interband-tunneling regime. A typical example is shown in Fig. 3 where the transmission spectra are plotted for the rectangular magnetic-electric barrier with  $U = 26$ . From Fig. 3(e) one can see that in the barrier region it is the spin-up and/or spin-down valence band that overlaps with the same shadowed energy regime ( $15 < E < 25$ ). Since the spin-down valence band covers only a small portion of the shadowed region, the spin-down transmission is not remarkable, as shown in Figs. 3(c) and 3(d). The transmission  $T_{-\downarrow}$  is forbidden, while  $T_{+\downarrow}$  is visible only in a narrow energy interval around  $E = 15$  and  $E = 17$ . The total transmission is contributed to dominantly by spin-up electrons. One can also observe a series of valley-resolved transmission peaks in Figs. 3(a) and 3(b).




 FIG. 3. Same as in Fig. 2, but for the barrier height  $U = 26$ .

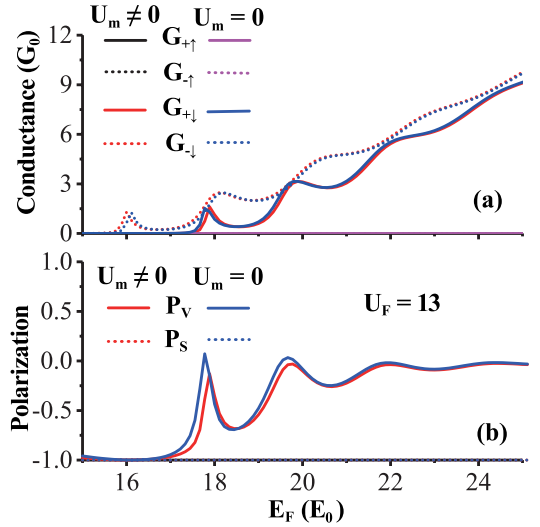
In the interband-tunneling case, the transmission peaks are narrow due to the spinor mismatching between propagating modes in barrier region and those in lead region.

In Fig. 3(f) the Landau levels in the middle region and dispersion of quasibound states are plotted. In the regime  $15 < E < 25$ , the Landau levels are derived from either the spin-up or spin-down valence band. The two quasibound states corresponding to resonant peaks in Fig. 3(c) arise from the two Landau levels  $E_{0,+↓} = 16.95$  and  $E_{1,+↓} = 15.83$ . For spin-up electrons in the  $\mathbf{K}$  valley, there exists a quasibound state with energy 23.0536 close to the zeroth Landau level  $E_{0,+↑} = 22.95$ . The corresponding resonant peak of  $T_{+↑}$  is sharp and does not appear in Fig. 3(a). Due to  $v_{↑} < v_{↓}$ , the distance between two nearest Landau levels ( $E_{n,-↑}$  and  $E_{n+1,+↑}$ ) is smaller than that (between  $E_{n,+↓}$  and  $E_{n+1,-↓}$ ) in Fig. 2(f). As a result, for spin-up electrons the quasibound states with different valley index are not well separated in energy.

In the absence of a valley-Zeeman term ( $U_m = 0$ ), although the Landau levels in Eq. (32) are valley-degenerate, the quasibound states are still valley-dependent, as shown in Table I. For a circular quantum dot based on gapped graphene, it was shown that [55] a perpendicular magnetic field leads to valley-resolved bound states under  $U_m = 0$ . The reason is that

 TABLE I. Energies of several quasibound states  $E_{QBS}(\tau)$  with  $q = 0$  and  $s = \uparrow$  under  $U = 26$  and  $U_m = 0$ .

Index	0	1	2	3	4	5
$E_{QBS}(\mathbf{K})$	22.95	21.82	20.63	19.27	17.74	16.09
$E_{QBS}(\mathbf{K}')$		21.91	20.87	19.71	18.36	16.83


 FIG. 4. (a) Valley and spin-resolved conductance and (b) polarization plotted as functions of the Fermi energy  $E_F$  for the realistic profile [depicted in Fig. 1(b)] of magnetic-electric barrier with  $U_F = 13$ . The calculations are made in the presence ( $U_m \neq 0$ ) or absence ( $U_m = 0$ ) of the valley-Zeeman coupling given by Eq. (6).

the magnetic field breaks degeneracies within different valleys while the confinement potential on gapped graphene breaks an effective time-reversal symmetry within each valley [55]. The same symmetry argument can be applied to the quasibound states considered in Table I.

Hereafter we turn to the realistic profile of magnetic-electric barrier. The smoothing electrostatic potential with maximum  $U_F$  is modeled as

$$U(x) = \frac{U_F}{2} \left[ \operatorname{erf}\left(\frac{x + L/2}{b} - 2\right) + \operatorname{erf}\left(\frac{-x + L/2}{b} - 2\right) \right], \quad (33)$$

where  $\operatorname{erf}(x)$  is the error function and  $b$  represents the width of the transition region. The structural parameters are chosen as  $L = 2$ ,  $h = 0.6$ ,  $z_0 = 0.01$ ,  $b = 0.1$ , and  $\mu_0 M = 2.4$  T [56]. The averaged magnetic field  $B_z$  in the region  $|x| < L/2$  is nearly 0.5 T. For the magnetic-electric barrier given by Eqs. (1) and (33) and depicted in Fig. 1(b), most transmission characteristics mentioned above remain.

In Fig. 4 we plot the valley and spin-resolved conductances and corresponding polarization as functions of the Fermi energy  $E_F$  for the barrier height  $U_F = 13$ . To examine the effect of the valley-Zeeman term given by Eq. (6), we also present results for the case  $U_m = 0$ . As shown in Fig. 4(a), the conductance of spin-up electrons are nearly zero in the considered interval of  $E_F$ , leading to a spin polarization  $\approx -100\%$ . In the energy interval  $16 < E_F < 17$ , the conductance  $G_{-↓}$  for spin-down electrons in the  $\mathbf{K}'$  valley exhibits a peak, while the conductance  $G_{+↓}$  for the valley  $\mathbf{K}$  is suppressed almost completely. A plateau of valley polarization  $\approx -100\%$  is thus observed in Fig. 4(b). With the increase of  $E_F$ , both  $G_{-↓}$  and  $G_{+↓}$  increase in an oscillating way. These observations reflect the features in the transmission spectrum shown in Fig. 2. The valley polarization is always negative. It has sev-

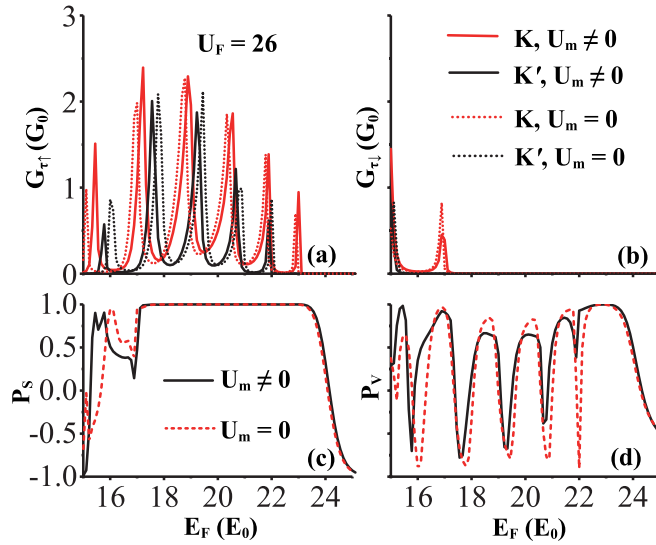


FIG. 5. Conductance and polarization plotted as functions of Fermi energy  $E_F$  for the realistic profile [depicted in Fig. 1(b)] of magnetic-electric barrier with  $U_F = 26$ . (a,b) Valley-resolved conductances  $G_{\tau\uparrow}$  and  $G_{\tau\downarrow}$  for spin-up and spin-down electrons; (c) spin polarization  $P_S$ ; (d) valley polarization  $P_V$ .

eral dips with decreasing depth. The amplitude of the first dip around  $E_F = 18.5$  exceeds 60%. The valley conductance  $G_V$  has the greatest amplitude at this dip. In the absence of valley-Zeeman splitting, the conductance  $G_{\tau\downarrow}$  alters slightly its peak positions, while the polarization plateau and polarization dips almost unchanged. Accordingly, for the transport in the intraband-tunneling regime the valley-Zeeman splitting has a minor effect on the valley polarization.

In the case of interband tunneling, the valley-Zeeman splitting can change greatly the conductance and polarization, as shown in Fig. 5. Here the calculations are made for the magnetic-electric barrier depicted in Fig. 1(b) with  $U_F = 26$ . For spin-up electrons, the conductance exhibits several valley-resolved peaks with large peak-to-trough ratio. The conductance for spin-down electrons is remarkable only for  $E_F$  near 15 or 17, which is mainly contributed to by the  $\mathbf{K}$  branch. These observations can be understood from Fig. 3. The inclusion of valley-Zeeman splitting shifts the peaks of  $G_{-\uparrow}$  towards the low-energy region and lifts the peak positions of  $G_{+\uparrow}$ . The change of peak positions is more remarkable for the first three peaks. For  $15 < E_F < 17$ , the spin polarization changes quickly from a value  $\approx -100\%$  to a value  $\approx +100\%$  and is affected obviously by the valley-Zeeman term. For  $17 < E_F < 23$ , the spin polarization is nearly 100%. For  $23 < E_F < 25$ , the spin-down intraband tunneling dominates gradually over the spin-up interband tunneling so that the spin polarization changes from a value  $\approx +100\%$  to a value  $\approx -100\%$ . In the presence of valley-Zeeman splitting, the valley polarization  $P_V$  approaches 100% near some peaks of  $G_{+\uparrow}$  or  $G_{+\downarrow}$ . It is lower than  $-70\%$  near the first two peaks of  $G_{-\uparrow}$ . When the valley-Zeeman term is removed, all troughs of  $P_V$  move down (some close to  $-90\%$ ) and shift to the right. It is seen that the valley-Zeeman term can enhance the valley polarization near the first peak of  $P_V$  and almost unchanged the

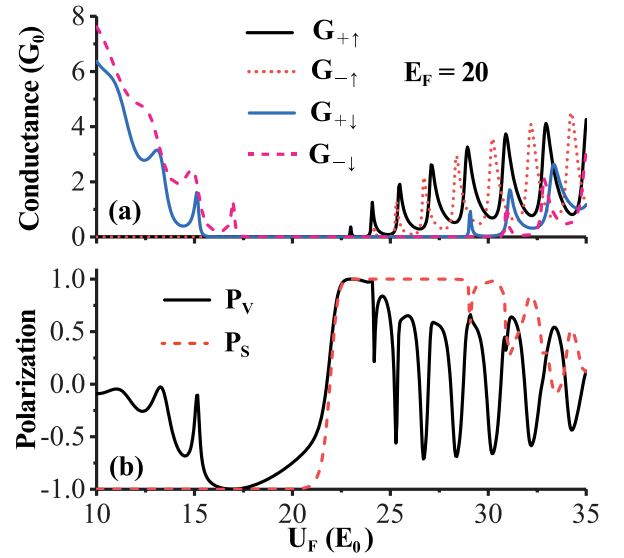


FIG. 6. (a) Valley and spin-resolved conductance and (b) polarization plotted as functions of electric barrier height  $U_F$ . The Fermi energy is set at  $E_F = 20$ .

peak near  $E_F = 17$ . In other cases, the valley-Zeeman term can reduce the amplitude of  $P_V$ .

Finally, we examine the voltage tunability of spin and valley-resolved conductance and related polarization. In Fig. 6 we plot  $G_{\tau s}$ ,  $P_S$ , and  $P_V$  as functions of electric barrier height  $U_F$ . The Fermi energy is fixed at  $E_F = 20$ . In the considered interval of  $U_F$ , the spin-up conductance  $G_{\pm\uparrow}$  is suppressed for  $U_F < 23$  while the spin-down conductance  $G_{\pm\downarrow}$  almost vanishes for  $17.3 < U_F < 29$  [see Fig. 6(a)]. The reason is that the propagating modes are absent in the scattering region when  $|E_F - U_F - D_s| < \Delta_s$ . Accordingly, the spin polarization is nearly  $-100\%$  for  $10 < U_F < 17.3$  and  $+100\%$  for  $23 < U_F < 29$  [see Fig. 6(b)]. For  $29 < U_F < 35$ , the spin-up and spin-down propagating modes can coexist in the scattering region, leading to an oscillating decay of  $P_S$  with  $U_F$ . For  $10 < U_F < 17.3$ , the transport is in the intraband-tunneling regime. The conductance  $G_{\pm\downarrow}$  shows valley-dependent peaks, troughs, and the upper cutoff. The corresponding valley polarization is negative and has two troughs. It approaches  $-100\%$  near the last peak ( $U_F \approx 17$ ) of  $G_{-\downarrow}$ . For  $23 < U_F < 29$ , the transport is dominated by interband tunneling. As  $U_F$  increases, the valley-resolved peaks and troughs of  $G_{\pm\uparrow}$  move up. The maximum of  $P_V$  is close to 100% near the first two peaks of  $G_{+\uparrow}$ . For  $24.5 < U_F < 33.5$ , the valley polarization has peaks higher than 50% and troughs lower than  $-50\%$ . For  $U_F > 29$ , the spin-down conductance  $G_{\pm\downarrow}$  becomes noticeable. Near the peaks of  $G_{+\downarrow}$ , the valley polarization reaches maximum at the minimum of spin polarization. The considered range of barrier height  $U_F \in [0.081, 0.284]$  eV is experimentally feasible [57,58].

#### IV. CONCLUSION

In summary, we investigated the valley-dependent and spin-resolved transport properties of electrons in graphene coupling to a neighboring FI film. The FI is thick only in a

stripe region and generates a local magnetic field. Because the exchange-proximity interaction brings a sublattice-staggered potential and spin-dependent gap opening, we found that such a local magnetic field enables spin-resolved valley filtering. One related mechanism is valley-resolved quasibound states created by magnetic-electric barrier and sublattice-staggered potential. Another mechanism is valley-Zeeman coupling between the magnetic field and orbital magnetic moment. When the transport is in the intraband-tunneling regime, both the spin and valley polarization are almost complete ( $\approx -100\%$ ) in a window of Fermi energy. The valley-Zeeman coupling plays a minor role in this case. In the interband-tunneling transport regime, the valley polarization oscillates with the

Fermi energy and can approach 100% or  $-70\%$  near some conductance peaks. The spin polarization is near 100% in a wide window of Fermi energy. In this case, the valley-Zeeman coupling can greatly affect the spin and valley polarization. We also showed that both the spin and valley polarization can be tuned by gate voltages. Our results could shed some light on exploring additional functions of graphene-based devices under a magnetic proximity.

#### ACKNOWLEDGMENT

This work was supported by the National Natural Science Foundation of China (Grant No. 11774314).

- 
- [1] B. Trauzettel, D. V. Bulaev, D. Loss, and G. Burkard, Spin qubits in graphene quantum dots, *Nat. Phys.* **3**, 192 (2007).
- [2] D. Huertas-Hernando, F. Guinea, and A. Brataas, Spin-orbit coupling in curved graphene, fullerenes, nanotubes, and nanotube caps, *Phys. Rev. B* **74**, 155426 (2006).
- [3] D. Liu, Y. Hu, H. Guo, and X. F. Han, Magnetic proximity effect at the molecular scale: First-principles calculations, *Phys. Rev. B* **78**, 193307 (2008).
- [4] H. Haugen, D. Huertas-Hernando, and A. Brataas, Spin transport in proximity-induced ferromagnetic graphene, *Phys. Rev. B* **77**, 115406 (2008).
- [5] P. Michetti and P. Recher, Spintronics devices from bilayer graphene in contact to ferromagnetic insulators, *Phys. Rev. B* **84**, 125438 (2011).
- [6] I. Vobornik, U. Manju, J. Fujii, F. Borgatti, P. Torelli, D. Krizmancic, Y. S. Hor, R. J. Cava, and G. Panaccione, Magnetic proximity effect as a pathway to spintronic applications of topological insulators, *Nano Lett.* **11**, 4079 (2011).
- [7] Z. Wang, C. Tang, R. Sachs, Y. Barlas, and J. Shi, Proximity-Induced Ferromagnetism in Graphene Revealed by the Anomalous Hall Effect, *Phys. Rev. Lett.* **114**, 016603 (2015).
- [8] A. Hallal, F. Ibrahim, H. Yang, S. Roche, and M. Chshiev, Tailoring magnetic insulator proximity effects in graphene: First-principles calculations, *2D Mater.* **4**, 025074 (2017).
- [9] B. Uchoa, V. N. Kotov, N. M. R. Peres, and A. H. Castro Neto, Localized Magnetic States in Graphene, *Phys. Rev. Lett.* **101**, 026805 (2008).
- [10] O. V. Yazyev and L. Helm, Defect-induced magnetism in graphene, *Phys. Rev. B* **75**, 125408 (2007).
- [11] G. Z. Magda, X. Jin, I. Hagymási, P. Vancsó, Z. Osváth, P. Nemes-Incze, C. Hwang, L. P. Biro, and L. Tapasztó, Room-temperature magnetic order on zigzag edges of narrow graphene nanoribbons, *Nature (London)* **514**, 608 (2014).
- [12] J. Munárriz, F. Domínguez-Adame, P. A. Orellana, and A. V. Malyshev, Graphene nanoring as a tunable source of polarized electrons, *Nanotechnology* **23**, 205202 (2012).
- [13] E. Díaz, K. Miralles, F. Domínguez-Adame, and C. Gaul, Spin-dependent terahertz oscillator based on hybrid graphene superlattices, *Appl. Phys. Lett.* **105**, 103109 (2014).
- [14] H. Savin, P. Kuivalainen, N. Lebedeva, and S. Novikov, Spin disorder scattering in a ferromagnetic insulator-on-graphene structure, *Phys. Status Solidi B* **251**, 407 (2014).
- [15] Y. Song and G. Dai, Spin filter and spin valve in ferromagnetic graphene, *Appl. Phys. Lett.* **106**, 223104 (2015).
- [16] M. Saiz-Bretín, J. Munárriz, A. V. Malyshev, and F. Domínguez-Adame, Control of spin-polarized currents in graphene nanorings, *Phys. Lett. A* **379**, 2102 (2015).
- [17] D. V. Averyanov, I. S. Sokolov, A. M. Tokmachev, O. E. Parfenov, I. A. Karateev, A. N. Taldenkov, and V. G. Storchak, High-temperature magnetism in graphene induced by proximity to EuO, *ACS Appl. Mater. Interfaces* **10**, 20767 (2018).
- [18] J. C. Leutenantsmeyer, A. A. Kaverzin, M. Wojtaszek, and B. J. Van Wees, Proximity induced room temperature ferromagnetism in graphene probed with spin currents, *2D Mater.* **4**, 014001 (2017).
- [19] V. T. Phong, N. R. Walet, and F. Guinea, Effective interactions in a graphene layer induced by the proximity to a ferromagnet, *2D Mater.* **5**, 014004 (2018).
- [20] H. X. Yang, A. Hallal, D. Terrade, X. Waintal, S. Roche, and M. Chshiev, Proximity Effects Induced in Graphene by Magnetic Insulators: First-Principles Calculations on Spin Filtering and Exchange-Splitting Gaps, *Phys. Rev. Lett.* **110**, 046603 (2013).
- [21] D. R. Klein, D. MacNeill, J. L. Lado, D. Soriano, E. Navarro-Moratalla, K. Watanabe, T. Taniguchi, S. Manni, P. Canfield, J. Fernández-Rossier, and P. Jarillo-Herrero, Probing magnetism in 2D van der Waals crystalline insulators via electron tunneling, *Science* **360**, 1218 (2018).
- [22] Y. Song, Electric-field-induced extremely large change in resistance in graphene ferromagnets, *J. Phys. D: Appl. Phys.* **51**, 025002 (2018).
- [23] D. A. Solis, A. Hallal, X. Waintal, and M. Chshiev, Proximity magnetoresistance in graphene induced by magnetic insulators, *Phys. Rev. B* **100**, 104402 (2019).
- [24] M. Evelt, H. Ochoa, O. Dzyapko, V. E. Demidov, A. Yurgens, J. Sun, Y. Tserkovnyak, V. Bessonov, A. B. Rinkevich, and S. O. Demokritov, Chiral charge pumping in graphene deposited on a magnetic insulator, *Phys. Rev. B* **95**, 024408 (2017).
- [25] P. Wei, S. Lee, F. Lemaitre, L. Pinel, D. Cutaia, W. Cha, F. Katmis, Y. Zhu, D. Heiman, J. Hone, J. S. Moodera, and C.-T. Chen, Strong interfacial exchange field in the graphene/EuS heterostructure, *Nat. Mater.* **15**, 711 (2016).
- [26] A. G. Swartz, P. M. Odenthal, Y. Hao, R. S. Ruoff, and R. K. Kawakami, Integration of the ferromagnetic insulator EuO onto graphene, *ACS Nano* **6**, 10063 (2012).

- [27] D. F. Förster, T. O. Wehling, S. Schumacher, A. Rosch, and T. Michely, Phase coexistence of clusters and islands: Europium on graphene, *New J. Phys.* **14**, 023022 (2012).
- [28] Z. Ge, S. Slizovskiy, F. Joucken, E. A. Quezada, T. Taniguchi, K. Watanabe, V. I. Falko, and J. Velasco, Control of Giant Topological Magnetic Moment and Valley Splitting in Trilayer Graphene, *Phys. Rev. Lett.* **127**, 136402 (2021).
- [29] Y. Lee, A. Knothe, H. Overweg, M. Eich, C. Gold, A. Kurzman, V. Klasovika, T. Taniguchi, K. Wantanabe, V. Fal'ko, T. Ihn, K. Ensslin, and P. Rickhaus, Tunable Valley Splitting due to Topological Orbital Magnetic Moment in Bilayer Graphene Quantum Point Contacts, *Phys. Rev. Lett.* **124**, 126802 (2020).
- [30] C. Park, Magnetoelectrically Controlled Valley Filter and Valley Valve in Bilayer Graphene, *Phys. Rev. Appl.* **11**, 044033 (2019).
- [31] C. Park, Valley filtering due to orbital magnetic moment in bilayer graphene, *Phys. Lett. A* **382**, 121 (2018).
- [32] K. S. Novoselov, A. K. Geim, S. V. Morozov, D. Jiang, M. I. Katsnelson, I. V. Grigorieva, S. V. Dubonos, and A. A. Firsov, Two-dimensional gas of massless dirac fermions in graphene, *Nature (London)* **438**, 197 (2005).
- [33] S. A. Vitale, D. Nezich, J. O. Varghese, P. Kim, N. Gedik, P. Jarillo-Herrero, D. Xiao, and M. Rothschild, Valleytronics: Opportunities, challenges, and paths forward, *Small* **14**, 1801483 (2018).
- [34] A. Rycercz, J. Tworzdylo, and C. W. J. Beenakker, Valley filter and valley valve in graphene, *Nat. Phys.* **3**, 172 (2007).
- [35] J. L. Garcia-Pomar, A. Cortijo, and M. Nieto-Vesperinas, Fully Valley-Polarized Electron Beams in Graphene, *Phys. Rev. Lett.* **100**, 236801 (2008).
- [36] S. P. Milovanović and F. M. Peeters, Strain controlled valley filtering in multi-terminal graphene structures, *Appl. Phys. Lett.* **109**, 203108 (2016).
- [37] F. Zhai and K. Chang, Valley filtering in graphene with a dirac gap, *Phys. Rev. B* **85**, 155415 (2012).
- [38] S. A. Oliaei Motlagh, F. Nematollahi, V. Apalkov, and M. I. Stockman, Topological resonance and single-optical-cycle valley polarization in gapped graphene, *Phys. Rev. B* **100**, 115431 (2019).
- [39] A. M. Khalifa, R. K. Kaul, E. Shimshoni, H. A. Fertig, and G. Murthy, Weyl Semimetal Path to Valley Filtering in Graphene, *Phys. Rev. Lett.* **127**, 126801 (2021).
- [40] A. Nogaret, Electron dynamics in inhomogeneous magnetic fields, *J. Phys.: Condens. Matter* **22**, 253201 (2010).
- [41] A. Tarasov, S. Hugger, H. Xu, M. Cerchez, T. Heinzl, I. V. Zozoulenko, U. Gasser-Szerer, D. Reuter, and A. D. Wieck, Quantized Magnetic Confinement in Quantum Wires, *Phys. Rev. Lett.* **104**, 186801 (2010).
- [42] B. Schüler, M. Cerchez, H. Xu, J. Schluck, T. Heinzl, D. Reuter, and A. D. Wieck, Observation of quantum states without a semiclassical equivalence bound by a magnetic field gradient, *Phys. Rev. B* **90**, 201111(R) (2014).
- [43] M. Cerchez, T. Chirila, H. Bettermann, B. Schüler, and T. Heinzl, Collimation of electrons at closed magnetic barriers in two-dimensional electron gases, *Phys. Rev. B* **99**, 085303 (2019).
- [44] I. S. Ibrahim and F. M. Peeters, Two-dimensional electrons in lateral magnetic superlattices, *Phys. Rev. B* **52**, 17321 (1995).
- [45] D. Xiao, W. Yao, and Q. Niu, Valley-Contrasting Physics in Graphene: Magnetic Moment and Topological Transport, *Phys. Rev. Lett.* **99**, 236809 (2007).
- [46] Y. Takehito, Controllable valley and spin transport in ferromagnetic silicene junctions, *Phys. Rev. B* **87**, 241409(R) (2013).
- [47] Y. Wang, Resonant spin and valley polarization in ferromagnetic silicene quantum well, *Appl. Phys. Lett.* **104**, 032105 (2014).
- [48] Z. Niu and S. Dong, Valley and spin thermoelectric transport in ferromagnetic silicene junctions, *Appl. Phys. Lett.* **104**, 202401 (2014).
- [49] H. Xu, Scattering-matrix method for ballistic electron transport: Theory and an application to quantum antidot arrays, *Phys. Rev. B* **50**, 8469 (1994).
- [50] F. Zhai and J. Lu, General relation between the group delay and dwell time in multicomponent electron systems, *Phys. Rev. B* **94**, 165426 (2016).
- [51] I. S. Gradshteyn and I. M. Ryzhik, *Table of Integrals, Series, and Products* (Academic Press, New York, 1980).
- [52] F. D. M. Haldane, Model for a Quantum Hall Effect without Landau Levels: Condensed-Matter Realization of the "Parity Anomaly", *Phys. Rev. Lett.* **61**, 2015 (1988).
- [53] J. N. Fuchs and P. Lederer, Spontaneous Parity Breaking of Graphene in the Quantum Hall Regime, *Phys. Rev. Lett.* **98**, 016803 (2007).
- [54] H. C. Nguyen, M. T. Hoang, and V. L. Nguyen, Quasi-bound states induced by one-dimensional potentials in graphene, *Phys. Rev. B* **79**, 035411 (2009).
- [55] P. Recher, J. Nilsson, G. Burkard, and B. Trauzettel, Bound states and magnetic field induced valley splitting in gate-tunable graphene quantum dots, *Phys. Rev. B* **79**, 085407 (2009).
- [56] C. Caspers, M. Müller, A. X. Gray, A. M. Kaiser, A. Gloskovskii, C. S. Fadley, W. Drube, and C. M. Schneider, Chemical stability of the magnetic oxide  $\text{e}_\text{u}$  directly on silicon observed by hard x-ray photoemission spectroscopy, *Phys. Rev. B* **84**, 205217 (2011).
- [57] J. Liu, Q. Li, Y. Zou, Q. Qian, Y. Jin, G. Li, K. Jiang, and S. Fan, The dependence of graphene raman D-band on carrier density, *Nano Lett.* **13**, 6170 (2013).
- [58] H. Hu, F. Zhai, D. Hu, Z. Li, B. Bai, X. Yang, and Q. Dai, Broadly tunable graphene plasmons using an ion-gel top gate with low control voltage, *Nanoscale* **7**, 19493 (2015).